Spectral Precoding Integration in OTFS Modulation

Vahid Vahidpour, Roberto López-Valcarce
atlanTTic Research Center, Universidade de Vigo, Vigo, Spain
Email: {vahidpour,valcarce}@gts.uvigo.es

***Abstract*—Practical Orthogonal Time-Frequency-Space (OTFS) systems face excessive out-of-band radiation (OBR), which degrades overall network performance. We investigate the application of spectral precoding to cyclic prefix-based OTFS to mitigate OBR in high-mobility wireless channels, and propose a modification of the low-complexity delay-time domain maximal ratio combining iterative decoder to account for the spectral precoding operation at the transmitter. Simulation results demonstrate the effectiveness of the proposed scheme to mitigate OBR and improve bit error rate, showcasing its potential for high-mobility OTFS applications.**

***Index Terms*—OTFS, delay-Doppler, high mobility, out-of-band radiation, spectral precoding.**

I. Introduction

Future mobile communications will support global coverage and advanced applications in challenging, high-mobility scenarios. Orthogonal Frequency Division Multiplexing (OFDM) struggles with channel estimation in such dynamic settings, whereas the emerging Orthogonal Time-Frequency-Space (OTFS) modulation, operating in the delay-Doppler (DD) domain, offers robust performance by handling high Doppler spreads and time-varying channels consistently [1]–[3].

Ideally-pulsed OTFS systems were initially proposed in [4] to mitigate inter-carrier and inter-symbol interference (ICI/ISI) within the time-frequency (TF) domain, promising reliable receiver performance. However, these ideal systems are practically unrealizable. As an alternative, [5] showed that practical OTFS systems employing rectangular pulses with effective ICI/ISI cancellation can achieve comparable error performance. Rectangular pulse shaping, however, generates significant OBR, potentially causing adjacent channel interference and degrading communication quality. To address this issue, [6] proposes time-domain windowing at the transmitter by inserting designed guards between blocks and applying windowing. While effective, this technique substantially reduces data throughput. Thus, efficient spectral sidelobe suppression is crucial in designing rectangularly pulsed OTFS systems.

Various techniques, including filtering [7], windowing [8], [9], active interference cancellation (AIC) [10], [11], and spectral precoding [12]–[16], have been proposed for rectangularly pulsed OFDM. Although these methods have shown promise in OFDM, their direct application to OTFS is not trivial, due to waveform modifications impacting demodulation. In particular, [17] introduces an initial spectral precoding stage to suppress sidelobes and reduce peak-to-average power ratio (PAPR), with modifications to further improve PAPR presented in [18]. In these works, symbol detection at the receiver is based on linear minimum mean square error (LMMSE) equalization in the time domain, followed by spectral decoding and symbol decision in the DD domain. Nevertheless, to the best of our knowledge, the adaptation of more sophisticated OTFS detectors to handle spectral precoding has not been addressed yet.

Motivated by the good properties of the maximum ratio combining (MRC) detector, which enjoys low-complexity implementation without losing performance in OTFS systems [19], [20], we explore the applicability of such approach to spectrally precoded OTFS. Specifically, we focus on an OFDM-based implementation of OTFS [21], in which a cyclic prefix (CP) is prepended to every transmitted block. This is usually referred to as CP-OTFS, in contrast with the *reduced CP* implementation (RCP-OTFS) in which a CP is prepended to each frame (with a frame consisting of N blocks) [20], [22]. As in [17], we assume a spectral precoder operating on a per-block basis. We then appropriately modify the MRC detector to account for the action of the spectral precoder. The main contributions of the paper are summarized as follows:

- We explore the feasibility of applying spectral precoding, including orthogonal and AIC precoders, to mitigate the high OBR issue of CP-OTFS systems.
- We propose an iterative delay-time (DT) domain MRC detection scheme integrating spectral precoding.
- We assess the proposed detector across various precoding schemes, modulation orders, and frame sizes.
- Simulation results confirm substantial OBR reduction and reveal that the proposed detector outperforms other state-of-the-art detectors in terms of bit error rate (BER).

Notation: Vectors (resp. matrices) are represented with bold lowercase (resp. uppercase) symbols. $\mathbf{A}^*$, $\mathbf{A}^{\mathsf{T}}$, $\mathbf{A}^{\mathsf{H}}$, $\mathbf{A}^{\sharp}$ denote conjugate, transpose, conjugate transpose, and pseudoinverse of $\mathbf{A}$, resp. Symbols $\odot$ and $\oslash$ denote entry-wise product and division. The n-th column of the identity matrix is denoted as $\mathbf{e}_n$. $\mathsf{tr}(\mathbf{A})$ is the trace of $\mathbf{A}$, with $\mathsf{vec}(\mathbf{A})$ and $\mathsf{unvec}(\mathbf{a})$ denoting column-wise vectorization and reshaping. The $M \times M$ unitary Discrete Fourier transform (DFT) matrix is denoted by $\mathbf{F}_M$. $[a]_b$ denotes a modulo b. Sets $\mathcal{N} = \{0, \cdots, N-1\}$, $\mathcal{M} = \{0, \cdots, M-1\}$ define indices over N and M. $\mathsf{E}[\cdot]$ is the expectation operator, and $\mathsf{DEC}\{\cdot\}$ is the entry-wise hard-decision operator for a given constellation.

II. Spectrally-Precoded OTFS System Model

A. Transmitter

Fig. 1 depicts the block diagram of the OFDM-based spectrally precoded OTFS modulation and demodulation framework. Let $\mathbf{Q} \in \mathbb{C}^{D \times N}$ denote the frame of transmitted DD symbols, drawn from a suitable QAM constellation. This frame is spectrally precoded at coding rate $\rho = D/M < 1$ to generate the DD domain matrix $\mathbf{X}_{\mathrm{DD}} \in \mathbb{C}^{M \times N}$ as

$$\mathbf{X}_{\mathrm{DD}} = \bar{\mathbf{G}}\mathbf{Q}, \tag{1}$$

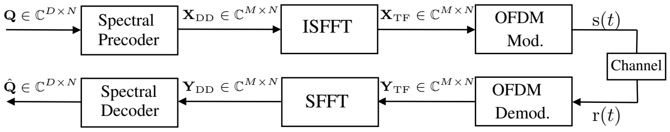

Fig. 1: OTFS system block diagram.

where $\bar{\mathbf{G}} \in \mathbb{C}^{M\times D}$ is the DD domain spectral precoder, with $M \geq D$; the precoding redundancy is $R = M - D$. Next, the TF domain matrix $\mathbf{X}_{\mathrm{TF}} \in \mathbb{C}^{M\times N}$ is computed by applying the inverse symplectic finite Fourier transform (ISFFT):

$$\mathbf{X}_{\mathrm{TF}} = \mathbf{F}_M \mathbf{X}_{\mathrm{DD}} \mathbf{F}_N^{\mathsf{H}}. \tag{2}$$

In particular, if $\mathbf{X}_{\mathrm{DD}}[l,k]$ denotes the (l,k)-th entry of $\mathbf{X}_{\mathrm{DD}}$, with $l \in \mathcal{M}$ and $k \in \mathcal{N}$ the delay and Doppler indices, then the (m,n)-th element of $\mathbf{X}_{\mathrm{TF}}$ is given by

$$\mathbf{X}_{\mathrm{TF}}[m,n] = \frac{1}{\sqrt{NM}} \sum_{l=0}^{M-1} \sum_{k=0}^{N-1} \mathbf{X}_{\mathrm{DD}}[l,k] \mathrm{e}^{\jmath 2\pi(\frac{nk}{N} - \frac{ml}{M})}, \tag{3}$$

with $n \in \mathcal{N}$ and $m \in \mathcal{M}$ the time and frequency indices, resp. The TF samples (2) are then fed to the OFDM transmitter on a column-by-column basis to synthesize the time-domain OTFS analog signal $\mathrm{s}(t)$. For this, the OFDM modulator may use an M-point inverse fast Fourier transform (IFFT) followed by CP insertion, increasing the sample rate $\frac{1}{T}$ at that point by an integer factor F, and a digital-to-analog conversion (DAC) stage with sampling rate $\frac{1}{T_s} = \frac{F}{T}$ samples/s; then, the subcarrier spacing is $\Delta_f = \frac{1}{MT}$ Hz, and its inverse $T_{\mathrm{u}} = MT$ is the duration in seconds of the useful part (i.e., not counting the CP duration $T_{\mathrm{cp}} = l_g T$) of the OFDM symbol. Note, in practice one must have $F > 1$ to allow for practical (i.e., non-ideal) interpolation filters in the DAC stage. Alternatively, the M-IFFT and upsampling steps can be replaced by a K-IFFT step with $K = F \cdot M$, as usual in practice [23]. Since the DAC still operates at $\frac{1}{T_s} = \frac{F}{T}$ samples/s, the subcarrier spacing $\frac{F}{KT} = \frac{1}{MT}$ remains the same.

On this basis, the baseband OTFS signal $\mathrm{s}(t)$ is obtained by digital-to-analog conversion of the sequence of samples obtained by sequentially reading out the columns of the matrix

$$\mathbf{A}_{\mathrm{CP}} \mathbf{F}_M^{\mathsf{H}} \mathbf{X}_{\mathrm{TF}} = \mathbf{A}_{\mathrm{CP}} \mathbf{X}_{\mathrm{DT}}, \quad \text{with } \mathbf{A}_{\mathrm{CP}} = \begin{bmatrix} \mathbf{0} & \mathbf{I}_{l_g} \\ \multicolumn{2}{c}{\mathbf{I}_M} \end{bmatrix}, \tag{4}$$

where $\mathbf{A}_{\mathrm{CP}} \in \mathbb{C}^{(M+l_g)\times M}$ is the CP insertion matrix, and $\mathbf{X}_{\mathrm{DT}} \in \mathbb{C}^{M\times N}$ is the DT domain matrix, satisfying

$$\mathbf{X}_{\mathrm{DT}} = \mathbf{X}_{\mathrm{DD}} \mathbf{F}_N^{\mathsf{H}} = \mathbf{F}_M^{\mathsf{H}} \mathbf{X}_{\mathrm{TF}}. \tag{5}$$

We define the vector $\mathbf{s} = \mathsf{vec}(\mathbf{X}_{\mathrm{DT}}) \in \mathbb{C}^{MN}$ such that $\mathbf{s}[m + nM] = \mathbf{X}_{\mathrm{DT}}[m,n]$, for $n \in \mathcal{N}$, $m \in \mathcal{M}$.

B. Receiver

At the receiver, the continuous-time received signal $\mathrm{r}(t)$ undergoes analog-to-digital conversion (ADC) at $\frac{1}{T}$ samples/s and CP removal, resulting in the discrete-time received sample vector $\mathbf{r} \in \mathbb{C}^{NM}$ with entries $\mathbf{r}[k]$, $k = 0, \cdots, MN-1$. This vector is reshaped into the DT domain matrix $\mathbf{Y}_{\mathrm{DT}} \in \mathbb{C}^{M\times N}$:

$$\mathbf{Y}_{\mathrm{DT}} = \mathsf{unvec}(\mathbf{r}) \quad \Leftrightarrow \quad \mathbf{Y}_{\mathrm{DT}}[m,n] = \mathbf{r}[m+nM], \tag{6}$$

for $n \in \mathcal{N}$, $m \in \mathcal{M}$. Then, the received TF domain matrix $\mathbf{Y}_{\mathrm{TF}} \in \mathbb{C}^{M\times N}$ is obtained by performing an M-point DFT along the columns of $\mathbf{Y}_{\mathrm{DT}}$:

$$\mathbf{Y}_{\mathrm{TF}} = \mathbf{F}_M \mathbf{Y}_{\mathrm{DT}}. \tag{7}$$

Subsequently, the DD domain matrix $\mathbf{Y}_{\mathrm{DD}} \in \mathbb{C}^{M\times N}$ is obtained by applying an SFFT to the TF domain matrix:

$$\mathbf{Y}_{\mathrm{DD}} = \mathbf{F}_M^{\mathsf{H}} \mathbf{Y}_{\mathrm{TF}} \mathbf{F}_N = \mathbf{Y}_{\mathrm{DT}} \mathbf{F}_N. \tag{8}$$

C. Channel

Consider a L-path time-varying channel, where the γ-th path is characterized by a complex gain g_γ, a normalized delay ℓ_γ, and a normalized Doppler κ_γ, with ℓ_γ, $\kappa_\gamma \in \mathbb{R}$. The actual delay (in s) and Doppler shift (in Hz) for the γ-th path are respectively given by

$$\tau_\gamma = \frac{\ell_\gamma}{M\Delta_f} \leq \tau_{\max}, \quad \nu_\gamma = \frac{\kappa_\gamma}{NT_{\mathrm{u}}},\ |\nu_\gamma| < \nu_{\max} \tag{9}$$

The maximum normalized delay is $\ell_{\max} = M\Delta_f \tau_{\max} \in \mathbb{R}$. We assume an underspread channel ($\tau_{\max}\nu_{\max} \ll 1$), where $\ell_{\max} < M$ and the Doppler range is bounded as $-\frac{N}{2} < \kappa_\gamma < \frac{N}{2}$. With the DD channel response $\mathrm{h_c}(\tau,\nu) = \sum_{\gamma=1}^{L} \mathrm{g}_\gamma \delta(\tau - \tau_\gamma)\delta(\nu - \nu_\gamma)$ [4], [24], the corresponding continuous time-varying channel impulse response is

$$\begin{aligned} \mathrm{g}(\tau,t) &= \int_\nu \mathrm{h_c}(\tau,\nu) \mathrm{e}^{\jmath 2\pi\nu(t-\tau)} \mathrm{d}\nu \\ &= \sum_{\gamma=1}^{L} \mathrm{g}_\gamma \delta(\tau - \tau_\gamma) \mathrm{e}^{\jmath 2\pi\nu_\gamma(t-\tau)}. \end{aligned} \tag{10}$$

The discrete-time baseband model is obtained by sampling the received signal $\mathrm{r}(t)$ at $t = d/M\Delta_f$, where $0 \leq d \leq NM-1$. Defining $\mathcal{L} = \{0, \cdots, l_{max}\}$ as a set of discrete delay taps representing delay shifts at integer multiples of the sampling period $T = 1/M\Delta_f$, the sampled baseband DT channel at discrete delay taps for all $l \in \mathcal{L}$ is given by [19], [25]

$$\mathrm{g}^s[l,d] \triangleq \mathrm{g}(lT, dT) = \sum_{\gamma=1}^{L} \mathrm{g}_\gamma z^{\kappa_\gamma(d-l)} \operatorname{sinc}(l - \ell_\gamma), \tag{11}$$

where $z = \mathrm{e}^{\jmath\frac{2\pi}{NM}}$. Fractional delays cause interference between channel responses due to sinc-based reconstruction at fractional delay points $\ell \in \mathcal{L}$ [25]. Practical systems, however; often ignore fractional delays, as the sampling resolution $1/M\Delta_f$ is typically sufficient to approximate delays to the nearest sampling points in wide-band systems [25]. Assuming integer multiples of $1/M\Delta_f$ for delays $\ell \in \mathbb{Z}$ the sinc function simplifies in (11) to $\delta[l - \ell_\gamma]$.

D. CP-OTFS: DT domain input-output relation

Let us write the DT matrices in (5) and (6) row-wise as

$$\mathbf{X}_{\mathrm{DT}} \triangleq [\,\tilde{\mathbf{x}}_0 \cdots \tilde{\mathbf{x}}_{M-1}\,]^{\mathsf{T}}, \quad \mathbf{Y}_{\mathrm{DT}} \triangleq [\,\tilde{\mathbf{y}}_0 \cdots \tilde{\mathbf{y}}_{M-1}\,]^{\mathsf{T}}, \tag{12}$$

where $\tilde{\mathbf{x}}_m$ and $\tilde{\mathbf{y}}_m$ are transmitted and received DT domain vectors with entries [22]

$$\tilde{\mathbf{x}}_m[n] = \mathbf{s}_n[m] \triangleq \mathbf{s}[m + nM], \tag{13}$$

$$\tilde{\mathbf{y}}_m[n] = \mathbf{r}_n[m] \triangleq \mathbf{r}[m + nM], \tag{14}$$

for $n \in \mathcal{N}$ and $m \in \mathcal{M}$. At the receiver, after removing the CP, we obtain the N time-domain vectors of size M as

$$\mathbf{r}_n[m] = \sum_l \mathrm{g}^s[l, m+nM_a]\mathbf{s}_n[[m-l]_M] + \widetilde{\mathbf{w}}_n[m] \quad (15)$$

with $M_a = M + l_g$ and $\tilde{\mathbf{w}}_n[m]$ the AWGN noise with variance $\sigma_{\tilde{w}}^2$. The corresponding DT input-output relation is [22]:

$$\tilde{\mathbf{y}}_m = \sum_{l \in \mathcal{L}} \tilde{\boldsymbol{\nu}}_{m,l} \odot \tilde{\mathbf{x}}_{[m-l]_M} + \tilde{\mathbf{w}}_n[m] \quad (16)$$

where $\tilde{\boldsymbol{\nu}}_{m,l}[n] = \mathrm{g}^s[l, m+nM_a]$ for $m \in \mathcal{M}$.

III. Spectral analysis of the OTFS signal

A. Spectral properties

We assume that the QAM symbols in a frame $\mathbf{Q}$ are zero-mean with unit variance and proper, i.e., for any $0 \le m \le D-1$ and $0 \le n \le N-1$ it holds that $\mathsf{E}[\mathbf{Q}[m,n]] = 0$ and

$$\mathsf{E}\big[|\mathbf{Q}[m,n]|^2\big] = 1, \quad \mathsf{E}\big[(\mathbf{Q}[m,n])^2\big] = 0. \quad (17)$$

QAM symbols are assumed uncorrelated within a given frame and also across frames. Then, in light of [26, Th. 1], the analog baseband OTFS signal is found to be cyclostationary with period equal to the total symbol duration $T_\mathrm{u} + T_\mathrm{cp}$, and its power spectral density (PSD) is essentially given by

$$\mathrm{P_s}(f) = |\mathrm{H_I}(f)|^2 \boldsymbol{\phi}^\mathsf{H}(f)\mathbf{G}\mathbf{G}^\mathsf{H}\boldsymbol{\phi}(f), \quad (18)$$

where $\mathbf{G} = \mathbf{F}_M \bar{\mathbf{G}}$ is the precoder in TF domain (since $\mathbf{X}_\mathrm{TF} = \mathbf{G}\mathbf{Q}\mathbf{F}_N^\mathsf{H}$), $\mathrm{H_I}(f)$ is the frequency response of the DAC interpolation filter (an analog lowpass filter with cutoff frequency $\frac{1}{2T_s}$), and $\boldsymbol{\phi}(f) \in \mathbb{C}^M$ is a vector with the responses of the active subcarriers, which for rectangular pulses of duration $T_\mathrm{u} + T_\mathrm{cp}$ are given by

$$\phi_m(f) = \frac{\mathrm{sinc}((f - m\Delta_f)T_s L)}{\mathrm{sinc}((f - m\Delta_f)T_s)} \mathrm{e}^{\jmath\pi(f - m\Delta_f)T_s(L-1)}, \quad (19)$$

with $L \triangleq (T_\mathrm{u} + T_\mathrm{cp})/T_s$ the total symbol duration in samples. Note, (19) is $\frac{1}{T_s}$-periodic in f; undesired replicas outside the signal passband will be attenuated by the DAC filter, see (18).

Let $\mathrm{W}(f) \ge 0 \ \forall f$ be a weighting function. The spectrally weighted power of the transmitted OTFS signal is then

$$\mathrm{P_W} \triangleq \int_{-\infty}^{+\infty} \mathrm{W}(f)\mathrm{P_s}(f)\mathrm{d}f \; = \; \mathsf{tr}\Big(\mathbf{G}^\mathsf{H}\boldsymbol{\Phi}\mathbf{G}\Big), \quad (20)$$

with the Hermitian positive semi-definite matrix $\boldsymbol{\Phi}$ defined as

$$\boldsymbol{\Phi} \triangleq \int_{-\infty}^{+\infty} \mathrm{W}(f)|H_\mathrm{I}(f)|^2 \boldsymbol{\phi}(f)\boldsymbol{\phi}^\mathsf{H}(f)\mathrm{d}f \ \ \in \mathbb{C}^{M\times M}. \quad (21)$$

By selecting $\mathrm{W}(f)$ appropriately, $\mathrm{P_W}$ can be made to correspond to a flexible definition of OBR, to be minimized. In the simplest case, to minimize OBR over a specific frequency set $\mathcal{B} \subset \mathbb{R}$, one sets $\mathrm{W}(f) = 1$ for $f \in \mathcal{B}$ and 0 elsewhere.

B. Spectral precoder designs

We explore two spectral precoder designs well studied in OFDM systems, namely AIC and orthogonal precoding. Both designs are posed as the minimization of $\mathrm{P_W}$ in (20) w.r.t. $\mathbf{G}$, but under different structural constraints on the TF-domain precoding matrix $\mathbf{G}$. With AIC [10], [11], the set of active subcarriers is split into a subset of D data subcarriers and a subset of $R = M - D$ cancellation subcarriers. Data is directly mapped to data subcarriers, whereas the cancellation subcarriers are modulated by an appropriate linear function of the data subcarriers in order to minimize OBR. This can be done by constraining the structure of the precoding matrix as follows. Let $\mathbf{E} \in \mathbb{C}^{M\times D}$ be the matrix comprising D columns of the identity matrix $\mathbf{I}_M$, corresponding to the indices of data subcarriers, and let $\mathbf{T} \in \mathbb{C}^{M\times R}$ comprise the remaining R columns, with the indices of cancellation subcarriers. Then

$$\mathbf{G} \triangleq \alpha\mathbf{E} + \mathbf{T}\boldsymbol{\Theta}, \quad (22)$$

where the matrix $\boldsymbol{\Theta} \in \mathbb{C}^{R\times D}$ is to be optimized. The scaling factor $\alpha \in (0, 1]$ is usually chosen to trade off sidelobe suppression and spectral peak regrowth, by adjusting the distribution of power between data and cancellation subcarriers. The problem is to minimize the OBR (20) under a cap on transmit power $\mathrm{P_T} = \mathsf{tr}\big(\mathbf{G}^\mathsf{H}\boldsymbol{\Phi}_\mathrm{T}\mathbf{G}\big)$, where $\mathrm{P_T}$ and $\boldsymbol{\Phi}_\mathrm{T}$ are obtained by setting $\mathrm{W}(f) = 1 \ \forall f$ in (20) and (21), respectively. Then the problem becomes

$$\min_{\boldsymbol{\Theta}} \mathrm{P_W} \quad \text{s. to } \mathrm{P_T} \le \mathrm{P_{max}}, \quad (23)$$

which can be efficiently solved, see [11]. The maximum transmit power $\mathrm{P_{max}}$ is taken as the transmit power of a baseline system without cancellation subcarrier insertion, i.e., with $(\alpha, \boldsymbol{\Theta}) = (1, \mathbf{0})$, so that $\mathrm{P_{max}} = \mathsf{tr}\big(\mathbf{E}^H\boldsymbol{\Phi}_\mathrm{T}\mathbf{E}\big)$.

In OFDM systems, AIC has the advantage of being transparent to the receiver, which merely discards the cancellation subcarriers; however, the amount of provided sidelobe suppression is limited. It can be improved with orthogonal precoding (OP) [12]–[14], in which columns of $\mathbf{G}$ are constrained to be orthonormal. The optimization problem becomes

$$\min_{\mathbf{G}} \mathrm{P_W} = \mathsf{tr}\big(\mathbf{G}^H\boldsymbol{\Phi}\mathbf{G}\big) \quad \text{s. to } \ \mathbf{G}^\mathsf{H}\mathbf{G} = \mathbf{I}_D, \quad (24)$$

whose solution comprises the eigenvectors corresponding to the D smallest eigenvalues of $\boldsymbol{\Phi}$. In OFDM systems, orthogonal structures usually outperform AIC precoders in terms of OBR reduction, but at the cost of not being transparent at the receiver side, where its effect needs to be taken into account in the demodulation process.

As seen above, the design of the TF domain precoder $\mathbf{G}$ in the OTFS transmitter is analogous to that for OFDM systems. However, because the detection process for OTFS is significantly different from that for OFDM, the impact of spectral precoding at the receiver needs to be investigated.

IV. Proposed Decoder

Building upon the input-output relations from Sec. II-D, we adapt the DT domain MRC algorithm initially proposed in [19] for ZP-OTFS and generalized in [20] to other OTFS formats, including CP-OTFS. In this context, the DT channel vectors $\{\tilde{\boldsymbol{\nu}}_{m,l}\}$, along with the received vectors $\{\tilde{\mathbf{y}}_m\}$, are used to iteratively estimate the rows $\{\tilde{\mathbf{x}}_m\}$ of the DT domain matrix $\mathbf{X}_{\text{DT}}$ as follows. First, we initialize estimates $\{\tilde{\mathbf{x}}_m^{(i)}, m \in \mathcal{M}\}$ for $i = 0$. Then, at iteration i, and for $m = 0, 1, \ldots, M-1$:

1) Compute residual noise-plus-interference (RNPI) vectors
$$\Delta\tilde{\mathbf{y}}_m^{(i)} = \tilde{\mathbf{y}}_m - \sum_{l\in\mathcal{L}} \tilde{\boldsymbol{\nu}}_{m,l} \odot \tilde{\mathbf{x}}_{[m-l]_M}^{(i)}. \tag{25}$$
2) Compute the residual error gradients $\Delta\tilde{\mathbf{g}}_m^{(i)}$, by aggregating the RNPI vectors $\Delta\tilde{\mathbf{y}}_{[m+l]_M}^{(i)}$ for $l \in \mathcal{L}$:
$$\Delta\tilde{\mathbf{g}}_m^{(i)} = \sum_{l\in\mathcal{L}} \tilde{\boldsymbol{\nu}}_{m+l,l}^* \odot \Delta\tilde{\mathbf{y}}_{[m+l]_M}^{(i)}. \tag{26}$$
3) With $\tilde{\mathbf{d}}_m = \sum_{l\in\mathcal{L}} \tilde{\boldsymbol{\nu}}_{m+l,l}^* \odot \tilde{\boldsymbol{\nu}}_{m+l,l}$, update the *soft estimates:*
$$\tilde{\mathbf{c}}_m^{(i)} = \tilde{\mathbf{x}}_m^{(i-1)} + \Delta\tilde{\mathbf{g}}_m^{(i)} \oslash \tilde{\mathbf{d}}_m. \tag{27}$$
4) To potentially replace the soft estimate with a hard estimate at point (i, m), construct the matrix $\mathbf{Z}_{i,m}$ as
$$\mathbf{Z}_{i,m} = [\,\tilde{\mathbf{x}}_0^{(i)} \cdots \tilde{\mathbf{x}}_{m-1}^{(i)}\, \tilde{\mathbf{c}}_m^{(i)}\, \tilde{\mathbf{x}}_{m+1}^{(i-1)} \cdots \tilde{\mathbf{x}}_{M-1}^{(i-1)}\,]^{\mathsf{T}}\mathbf{F}_N, \tag{28}$$
constituting the current estimate of $\mathbf{X}_{\text{DD}} = \bar{\mathbf{G}}\mathbf{Q}$. Then[1]
$$\boldsymbol{\Gamma}_{i,m} = \begin{cases} \mathbf{G}^{\mathsf{H}}\mathbf{F}_M\mathbf{Z}_{i,m}, & \text{for OP,} \\ \alpha^{-1}\mathbf{E}^{\mathsf{H}}\mathbf{F}_M\mathbf{Z}_{i,m}, & \text{for AIC,} \end{cases} \tag{29}$$
constitutes the current estimate of $\mathbf{Q}$. Thus, since the m-th row of $\mathbf{X}_{\text{DT}}$ is $\tilde{\mathbf{x}}_m = \mathbf{X}_{\text{DT}}^{\mathsf{T}}\mathbf{e}_m = \mathbf{F}_N^{\mathsf{H}}\mathbf{Q}^{\mathsf{T}}\bar{\mathbf{G}}^{\mathsf{T}}\mathbf{e}_m$, it can be estimated as $\mathbf{F}_N^{H}\mathsf{DEC}\{\boldsymbol{\Gamma}_{i,m}^{\mathsf{T}}\}\,\bar{\mathbf{G}}^{\mathsf{T}}\mathbf{e}_m$.
5) To improve both performance and convergence, a convex combination of soft and hard estimates is employed:
$$\tilde{\mathbf{x}}_m^{(i)} = (1-\lambda)\tilde{\mathbf{c}}_m^{(i)} + \lambda\mathbf{F}_N^{\mathsf{H}}\mathsf{DEC}\left\{\boldsymbol{\Gamma}_{i,m}^{\mathsf{T}}\right\}\boldsymbol{\zeta}_m, \tag{30}$$
with $\boldsymbol{\zeta}_m \triangleq \bar{\mathbf{G}}^{\mathsf{T}}\mathbf{e}_m$ and $\lambda \in [0, 1]$. Setting $\lambda = 0$ results in a purely soft estimate, while $\lambda = 1$ yields a hard estimate.
6) Update $\Delta\tilde{\mathbf{y}}_{[m+l]_M}^{(i)}$ using the most recent estimate $\tilde{\mathbf{x}}_m^{(i)}$.
7) Increment m and repeat steps 2 to 6 for $m \in \mathcal{M}$.
8) The algorithm terminates if the maximum number of iterations is reached or if the relative change in RNPI error norm drops below some threshold.

The computational complexity of step 4 above can be significantly reduced by noting that the matrices $\mathbf{Z}_{i,m}$ and $\mathbf{Z}_{i,m-1}$ differ only in their $(m-1)$-th and m-th rows, which allows to compute $\mathbf{Z}_{i,m}$ recursively. Specifically, letting
$$\boldsymbol{\varepsilon}_{i,m} \triangleq \tilde{\mathbf{c}}_m^{(i)} - \tilde{\mathbf{x}}_m^{(i)}, \qquad \boldsymbol{\delta}_{i,m} \triangleq \tilde{\mathbf{c}}_m^{(i)} - \tilde{\mathbf{x}}_m^{(i-1)}, \tag{31}$$
one has
$$\mathbf{Z}_{i,m} = \mathbf{Z}_{i,m-1} + (\mathbf{e}_m\boldsymbol{\delta}_{i,m}^{\mathsf{T}} - \mathbf{e}_{m-1}\boldsymbol{\varepsilon}_{i,m-1}^{\mathsf{T}})\mathbf{F}_N. \tag{32}$$
Thus, upon defining $\mathbf{f}_m \triangleq \bar{\mathbf{G}}^{\sharp}\mathbf{e}_m = \mathbf{G}^{\sharp}\mathbf{F}_M\mathbf{e}_m$, the following recursion is obtained, which is valid for OP and AIC[2]:
$$\boldsymbol{\Gamma}_{i,m} = \boldsymbol{\Gamma}_{i,m-1} + (\mathbf{f}_m\boldsymbol{\delta}_{i,m}^{\mathsf{T}} - \mathbf{f}_{m-1}\boldsymbol{\varepsilon}_{i,m-1}^{\mathsf{T}})\mathbf{F}_N. \tag{33}$$

The proposed method is summarized in Algorithm 1. For initialization, all $\tilde{\mathbf{x}}_m^{(0)}$ may be set to zero; or the low-complexity refined estimate from [22, p. 141] can be used instead. In the original DT-MRC detector (without spectral precoding), the term $\mathsf{DEC}\{\boldsymbol{\Gamma}_{i,m}^{\mathsf{T}}\}\,\boldsymbol{\zeta}_m$ in step (b) of Algorithm 1 is replaced by $\mathsf{DEC}\{\tilde{\mathbf{c}}_m^{(i)}\}$, whereas step (a) is not needed. The extra complexity incurred by these two steps is of $3ND + N\log_2(N)$ complex multiplications. Because of this, the computational complexity per iteration of the modified DT-MRC detector is $\mathcal{O}(NMD)$ for $\lambda > 0$, and $\mathcal{O}(NMl_g)$ for $\lambda = 0$ (same as the original DT-MRC scheme [20]). In contrast, the complexity of the LMMSE equalizer for CP-OTFS is $\mathcal{O}(NM^3)$, which can be reduced to $\mathcal{O}(NML^2)$ if the sparsity of the channel matrix is exploited [27].

Algorithm 1: DT-MRC detector w/spectral precoding

Input: $0 \le \lambda \le 1$, ϵ, $\bar{\mathbf{G}}$, $\tilde{\mathbf{d}}_m$, $\tilde{\mathbf{x}}_m^{(0)}$, $\tilde{\mathbf{y}}_m$, $\forall\, m \in \mathcal{M}$
for $m = 0 : M-1$ **do**
  $\Delta\tilde{\mathbf{y}}_m^{(0)} = \tilde{\mathbf{y}}_m - \sum_{l\in\mathcal{L}} \tilde{\boldsymbol{\nu}}_{m,l} \odot \tilde{\mathbf{x}}_{[m-l]_M}^{(0)}$;
end
for $i = 1$: *max iterations* **do**
  $\Delta\tilde{\mathbf{y}}^{(i)} = \Delta\tilde{\mathbf{y}}^{(i-1)}$;
  for $m = 0 : M-1$ **do**
    $\Delta\tilde{\mathbf{g}}_m^{(i)} = \sum_{l\in\mathcal{L}} \tilde{\boldsymbol{\nu}}_{m+l,l}^* \odot \Delta\tilde{\mathbf{y}}_{[m+l]_M}^{(i)}$;
    $\tilde{\mathbf{c}}_m^{(i)} = \tilde{\mathbf{x}}_m^{(i-1)} + \Delta\tilde{\mathbf{g}}_m^{(i)} \oslash \tilde{\mathbf{d}}_m$;
    $\boldsymbol{\Gamma}_{i,m} = \boldsymbol{\Gamma}_{i,m-1} + (\mathbf{f}_m\boldsymbol{\delta}_{i,m}^{\mathsf{T}} - \mathbf{f}_{m-1}\boldsymbol{\varepsilon}_{i,m-1}^{\mathsf{T}})\mathbf{F}_N$ (a);
    $\tilde{\mathbf{x}}_m^{(i)} = (1-\lambda)\tilde{\mathbf{c}}_m^{(i)} + \lambda\mathbf{F}_N^{\mathsf{H}}\mathsf{DEC}\left\{\boldsymbol{\Gamma}_{i,m}^{\mathsf{T}}\right\}\boldsymbol{\zeta}_m$ (b);
    for $l \in \mathcal{L}$ **do**
      $\Delta\tilde{\mathbf{y}}_{[m+l]_M}^{(i)} \leftarrow$
       $\Delta\tilde{\mathbf{y}}_{[m+l]_M}^{(i)} - \tilde{\boldsymbol{\nu}}_{m+l,l} \odot (\tilde{\mathbf{x}}_m^{(i)} - \tilde{\mathbf{x}}_m^{(i-1)})$;
    end
  end
  if $i >$ *min iterations* **then**
    if $|(\|\Delta\tilde{\mathbf{y}}^{(i)}\| - \|\Delta\tilde{\mathbf{y}}^{(i-1)}\|)|/\|\Delta\tilde{\mathbf{y}}^{(i-1)}\| < \epsilon$ **then**
      EXIT;
    end
  end
end
Output: $\hat{\mathbf{X}}_{\text{DD}} = \left[\tilde{\mathbf{x}}_0^{(i)} \cdots \tilde{\mathbf{x}}_{M-1}^{(i)}\right]^{\mathsf{T}}\mathbf{F}_N$, $\hat{\mathbf{Q}} = \mathsf{DEC}\left\{\bar{\mathbf{G}}^{\sharp}\hat{\mathbf{X}}_{\text{DD}}\right\}$

V. Simulation results

We consider a CP-OTFS system with 15-kHz subcarrier spacing and CP redundancy $T_{\text{cp}}/T_{\text{u}} = 1/16$, i.e., $T_{\text{cp}} = 1/16\Delta_f) = 4.167\ \mu$s. The channel follows the EVA model [28] with $L = 9$ paths, with the Doppler shift for each path is drawn from the uniform distribution $U(-\nu_{\max}, \nu_{\max})$, with $\nu_{\max}$ the maximum Doppler shift. We assume $NT_{\text{u}}\nu_{\max} = \kappa_{\max} = 4$. The maximum delay spread in terms of integer taps is set to be 5 ($l_{max} = 4$), so that $\tau_{max} \le T_{\text{cp}}$ for $M \ge 64$. We assume perfect channel state information at the receiver.

A. Power spectral density

To illustrate the effect of spectral precoding, consider a setting with $M = 128$ active subcarriers and an oversampling factor $F = 2$. The interpolation filter is assumed to be an ideal lowpass filter with cutoff frequency $\frac{1}{2T_s}$, and the OBR region is $\mathcal{B} = \left\{\frac{1}{4T_s} + \frac{\Delta f}{2} \le |f| \le \frac{1}{2T_s}\right\}$. We adopt a flat weighting function $W(f) = 1$ for $f \in \mathcal{B}$ and zero otherwise.

Fig. 2 depicts the PSDs obtained from different precoder schemes, all with a precoder redundancy $R = 8$. Thus, with

[1]Recall that, for AIC, one has $\mathbf{G} = \alpha\mathbf{E} + \mathbf{T}\boldsymbol{\Theta}$, with $\mathbf{E}^{\mathsf{H}}\mathbf{E} = \mathbf{I}_D$ and $\mathbf{E}^{\mathsf{H}}\mathbf{T} = \mathbf{0}$; thus, $\alpha^{-1}\mathbf{E}^{\mathsf{H}}\mathbf{G} = \mathbf{I}_D$, i.e., $\mathbf{G}^{\sharp} = \alpha^{-1}\mathbf{E}$.

[2]Note that $\mathbf{f}_m = \boldsymbol{\zeta}_m^*$ for OP, and $\mathbf{f}_m = \alpha^{-1}\mathbf{E}^{\mathsf{H}}\mathbf{F}_M\mathbf{e}_m$ for AIC.

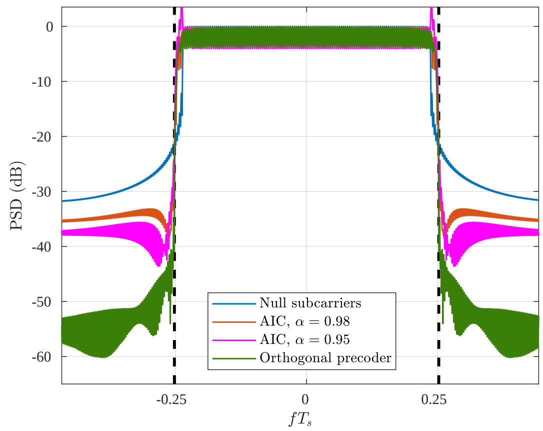

Fig. 2: PSDs for various precoder designs. $M = 128$, $N = 64$, $l_g = \lfloor \frac{M}{16} \rfloor$, $R = 6$, using 4-QAM.

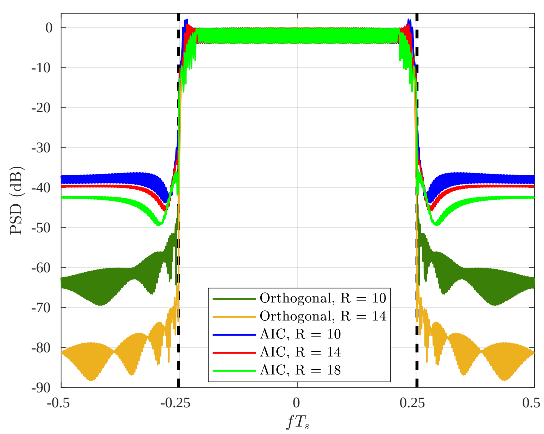

Fig. 3: PSDs for various precoder designs. $M = 128$, $N = 64$, $l_g = \lfloor \frac{M}{16} \rfloor$, for different values of R using 4-QAM.

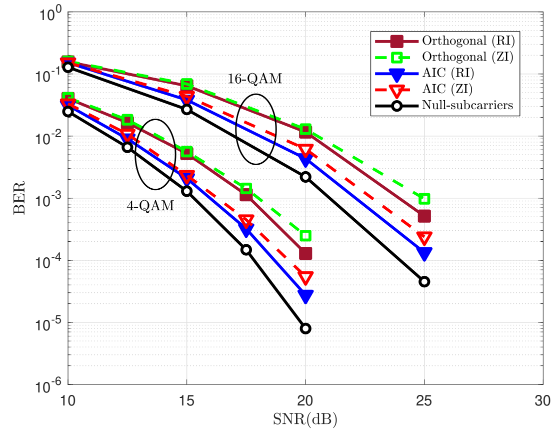

(a) $N = 32$, $M = 64$

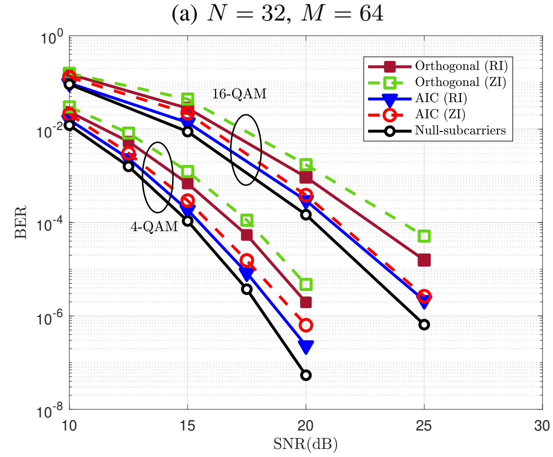

(b) $N = 64$, $M = 128$

Fig. 4: BER for different precoders and frame sizes. $\lambda = 0.2$

AIC, 4 cancellation subcarriers are placed at each passband edge. With OP, the OBR is 25.6 dB lower than that of the unprecoded scheme with $R/2$ null subcarriers at each band edge (i.e., AIC with $\boldsymbol{\Theta} = \mathbf{0}$). For AIC, the OBR reduction is approximately 3.6 dB and 6.1 dB for $\alpha = 0.98$ and 0.95, resp.; as α increases, less power is allocated to cancellation subcarriers, leading to diminished OBR reduction. Conversely, decreasing α enhances OBR reduction, but cancellation subcarriers produce larger peaks in the PSD. Such spectral overshoots are undesirable in practice because spectral emission masks impose upper bounds on the PSD relative to its maximum value. Therefore, a trade-off must be found between OBR performance and spectral overshoot.

Fig. 3 shows the PSD for different redundancy R. In the orthogonal case, increasing R from 10 to 14 results in a substantial OBR decrease of about 20 dB. For the AIC precoder with α fixed at 0.96, it is evident that increasing R for a given α improves OBR reduction while reducing the magnitude of spectral peaks. Nevertheless, the sidelobe suppression capability of AIC is seen to be limited.

B. BER Performance

Fig. 4 shows BER curves (based on 10^3 frames per BER point) for the proposed detector with 4-QAM and 16-QAM, and with different spectral precoders with $R = 6$. The DT domain MRC detector is tested with an all-zeros initialization (ZI) and with the refined initialization (RI) from [22, p. 141]. Two different frame sizes are considered: $(N, M) = (32, 64)$ in Fig. 4(a), and $(N, M) = (64, 128)$ in Fig. 4(b). The improvement in BER with larger values of M and N is apparent and could be expected, since this improves the delay and Doppler resolutions. The use of the refined initialization is also seen to be beneficial in all cases. Regarding the impact of spectral precoding, a clear tradeoff is observed between OBR reduction and BER: although AIC has limited sidelobe suppression capability, it consistently exhibits a lower BER than OP; and even so, AIC still suffers from a BER loss with respect to the baseline null-subcarriers case.

Fig. 5 shows the BER performance of the proposed detector in terms of λ, assuming $(N, M) = (32, 64)$ and OP ($R = 6$). It is seen that $\lambda = 0.2$ yields close to optimal performance across SNR for both 4- and 16-QAM. The advantage of appropriately combining soft and hard estimates becomes more pronounced with higher SNR and/or denser constellations.

The performance of the proposed spectral precoding-aware DT-MRC decoder is compared with the approach from [17] (adapted to the CP-OTFS scenario), in which an LMMSE equalization step is first performed in the time domain, followed by mapping to the DD domain and then spectral decoding based on the pseudoinverse $\bar{\mathbf{G}}^\sharp$. Results are depicted in Fig. 6,

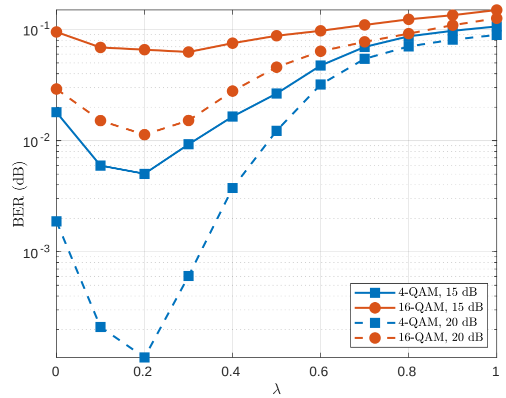

Fig. 5: BER performance of the DT-MRC detector as a function of λ. $N = 32$, $M = 64$, orthogonal precoder ($R = 6$).

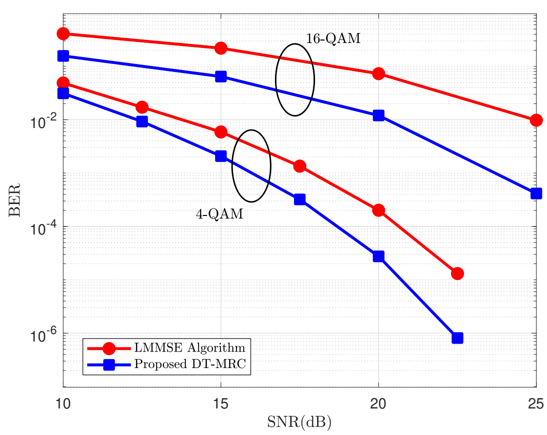

Fig. 6: BER performance: DT-MRC vs. LMMSE detectors. $N = 32$, $M = 64$, $\lambda = 0.2$, orthogonal precoder ($R = 6$).

showing the advantage of the proposed scheme.

VI. Conclusion

As for OFDM, incorporating spectral precoding in CP-OTFS systems is an effective way to reduce OBR; however, receiver operarion needs to be appropriately modified. The proposed DT-MRC detector achieves improved performance under spectral precoding with respect to previous LMMSE-based approaches, and with similar complexity. A tradeoff between OBR reduction and BER performance appears, with more powerful spectral precoders (e.g. orthogonal) showing a degradation in bit error rate.

Acknowledgment

Work funded by MCIN/AEI/10.13039/501100011033/ FEDER ”A way of making Europe” under project MAYTE (PID2022-136512OB-C22).

References

[1] Z. Wei, W. Yuan, S. Li, J. Yuan, G. Bharatula, R. Hadani, and L. Hanzo, “Orthogonal time-frequency space modulation: A promising next-generation waveform,” *IEEE Trans. Wireless Commun.*, vol. 28, no. 4, pp. 136–144, 2021.

[3] ——, “Delay-Doppler domain Tomlinson-Harashima precoding for OTFS-based downlink MU-MIMO transmissions: Linear complexity implementation and scaling law analysis,” *IEEE Trans. Commun.*, vol. 71, no. 4, pp. 2153–2169, 2023.

[2] S. Li et al., “A novel ISAC transmission framework based on spatially-spread orthogonal time frequency space modulation,” *IEEE J. Sel. Areas Commun.*, vol. 40, no. 6, pp. 1854–1872, 2022.

[4] R. Hadani, S. Rakib, M. Tsatsanis, A. Monk, A. J. Goldsmith, A. F. Molisch, and R. Calderbank, “Orthogonal time frequency space modulation,” in *2017 IEEE Wireless Communications and Networking Conference (WCNC)*, 2017, pp. 1–6.

[5] P. Raviteja, K. T. Phan, Y. Hong, and E. Viterbo, “Interference cancellation and iterative detection for orthogonal time frequency space modulation,” *IEEE Trans. Wireless Commun.*, vol. 17, no. 10, pp. 6501–6515, 2018.

[6] M. N. Hossain, Y. Sugiura, T. Shimamura, and H.-G. Ryu, “Waveform design of low complexity WR-OTFS system for the OOB power reduction,” in *2020 IEEE Wireless Commun. Netw. Conf. Workshops (WCNCW)*, 2020, pp. 1–5.

[7] M. Faulkner, “The effect of filtering on the performance of OFDM systems,” *IEEE Trans. Veh. Technol.*, vol. 49, pp. 1877–1884, 2000.

[8] K. Hussain and R. López-Valcarce, “Optimal window design for W-OFDM,” in *IEEE Int. Conf. Acoust., Speech Signal Process. (ICASSP)*, 2020, pp. 5275–5289.

[9] L. Díez, J. A. Cortés, F. J. Cañete, E. Martos-Naya, and S. Iranzo, “A generalized spectral shaping method for OFDM signals,” *IEEE Trans. Commun.*, vol. 67, no. 5, pp. 3540–3551, 2019.

[10] S. Brandes, I. Cosovic, and M. Schnell, “Reduction of out-of-band radiation in OFDM systems by insertion of cancellation carriers,” *IEEE Commun. Lett.*, vol. 10, no. 6, pp. 420–422, 2006.

[11] J. F. Schmidt, S. Costas-Sanz, and R. López-Valcarce, “Choose your subcarriers wisely: Active interference cancellation for cognitive OFDM,” *IEEE J. Emerg. Sel. Topics Circuits Syst.*, vol. 3, no. 4, pp. 615–625, 2013.

[12] M. Ma, X. Huang, B. Jiao, and Y. J. Guo, “Optimal orthogonal precoding for power leakage suppression in dft-based systems,” *IEEE Commun. Lett.*, vol. 59, no. 3, pp. 844–853, 2011.

[13] I. V. L. Clarkson, “Orthogonal precoding for sidelobe suppression in DFT-based systems using block reflectors,” in *Proc. IEEE Int. Conf. Acoust., Speech, Signal Process.*, 2017, pp. 3709–3713.

[14] K. Hussain and R. López-Valcarce, “Orthogonal precoding with memory for sidelobe suppression in OFDM,” in *2022 30th Eur. Signal Process. Conf. (EUSIPCO)*, 2022, pp. 1646–1650.

[15] C.-D. Chung and K.-W. Chen, “Spectrally precoded OFDM without guard insertion,” *IEEE Trans. Veh. Technol.*, vol. 66, no. 1, pp. 107–121, 2017.

[16] K. Hussain, R. López-Valcarce, F. Rey, J. Sala-Alvarez, and J. Villares, “Sidelobe suppression for multicarrier signals via structured spectral precoding,” *IEEE Trans. Commun.*, vol. 72, no. 6, pp. 3155–3168, 2024.

[17] W.-C. Chen, C.-H. Lu, and C.-D. Chung, “Spectrally precoded OTFS modulation,” in *IEEE 96th Veh. Technol. Conf. (VTC-Fall)*, 2022.

[18] Y. Zhu, Z. Wang, and Z. Liu, “Optimal column inversion precoding for PAPR reduction in SP-OTFS system,” in *2024 IEEE/CIC Int. Conf. Commun. China (ICCC Workshops)*, 2024, pp. 553–557.

[19] T. Thaj and E. Viterbo, “Low complexity iterative rake decision feedback equalizer for zero-padded OTFS systems,” *IEEE Trans. Veh. Technol.*, vol. 69, no. 12, pp. 15 606–15 622, 2020.

[20] T. Thaj, E. Viterbo, and Y. Hong, “General I/O relations and low-complexity universal MRC detection for all OTFS variants,” *IEEE Access*, vol. 10, pp. 96 026–96 037, 2022.

[21] A. Farhang, A. RezazadehReyhani, L. E. Doyle, and B. Farhang-Boroujeny, “Low complexity modem structure for OFDM-based orthogonal time frequency space modulation,” *IEEE Wireless Commun. Lett.*, vol. 7, no. 3, pp. 344–347, 2018.

[22] Y. Hong, T. Thaj, and E. Viterbo, *Delay-Doppler Communications: Principles and Applications*. Academic Press, 2022.

[23] B. Farhang-Boroujeny, *Signal Processing Techniques for Software Radios*. Lulu Publishing House, 2010.

[24] P. Raviteja, Y. Hong, E. Viterbo, and E. Biglieri, “Practical pulse-shaping waveforms for reduced-cyclic-prefix OTFS,” *IEEE Trans. Veh. Technol.*, vol. 68, no. 1, pp. 957–961, 2019.

[25] D. Tse and P. Viswanath, *Fundamentals of Wireless Communication*. Cambridge University Press, 2005.

[26] R. López-Valcarce, “General form of the power spectral density of multicarrier signals,” *IEEE Commun. Lett.*, vol. 26, no. 8, pp. 1755–1759, 2022.

[27] S. Tiwari, S. S. Das, and V. Rangamgari, “Low complexity LMMSE receiver for OTFS,” *IEEE Commun. Lett.*, vol. 23, no. 12, pp. 2205–2209, 2019.

[28] “LTE evolved universal terrestrial radio access (E-UTRA); base station (BS) radio transmission and reception,” *3GPP TS 36.104 version 8.6.0 Release 8*, Jul. 2009.